

Alloying effect-induced electron polarization drives nitrate reduction to ammonia

Haibo Yin

Tsinghua University

Yue Peng

Tsinghua University <https://orcid.org/0000-0001-5772-3443>

Shangchao Xiong

Tsinghua University

Jianjun Chen

Tsinghua University <https://orcid.org/0000-0003-4730-7803>

Chizhong Wang

Tsinghua University

Rong Wang

Tsinghua University

Zhen Chen

Tsinghua University

Yasutaka Kuwahara

Osaka University <https://orcid.org/0000-0002-5867-6463>

Jingshan Luo

Nankai University <https://orcid.org/0000-0002-1770-7681>

Hiromi Yamashita

Osaka University

Junhua Li (✉ lijunhua@tsinghua.edu.cn)

Tsinghua University

Article

Keywords: electron polarization, nitrate reduction, ammonia

Posted Date: December 10th, 2020

DOI: <https://doi.org/10.21203/rs.3.rs-118696/v1>

License:   This work is licensed under a Creative Commons Attribution 4.0 International License.

[Read Full License](#)

1 Alloying effect-induced electron polarization drives nitrate reduction to ammonia

2
3 Haibo Yin^a, Yue Peng^a, Shangchao Xiong^a, Jianjun Chen^a, Chizhong Wang^a, Rong Wang^a,
4 Zhen Chen^a, Yasutaka Kuwahara^b, Jingshan Luo^c, Hiromi Yamashita^b, Junhua Li^{a*}

5
6
7 a State Key Joint Laboratory of Environment Simulation and Pollution Control, School of
8 Environment, Tsinghua University, Beijing, 100084, PR China

9 b Division of Materials and Manufacturing Science, Graduate School of Engineering, Osaka
10 University, Osaka, 565-0871, Japan.

11 c Institute of Photoelectronic Thin Film Devices and Technology, Solar Energy Research Center,
12 Key Laboratory of Photoelectronic Thin Film Devices and Technology of Tianjin, Ministry of
13 Education Engineering Research Center of Thin Film Photoelectronic Technology, Nankai
14 University, Tianjin, 300350, PR China

15
16
17
18 Corresponding e-mails:

19 lijunhua@tsinghua.edu.cn;

20

21

22

23

24 **Abstract**

25 Electrochemical conversion of nitrate (NO_3^-) to ammonia (NH_3) holds significant potential in
26 the control of nitrogen oxide (NO_x) from stationary sources. However, previous studies on reaction
27 intermediates remain unclear. Here we report that Pd/Cu₂O hybrids with mesoporous hollow
28 sphere structure show high selectivity (96.70%) and Faradaic efficiency (94.32%) for NH_3
29 synthesis from NO_3^- . Detailed characterizations demonstrate that (1) Pd enables electrons transfer
30 ($\text{Pd } 3d \rightarrow \text{Cu } 3d$) and makes the polarization of Cu 3d orbitals by forming partial PdCu alloys,
31 which makes Pd electron-deficiency but offers empty orbits to adsorb NO_3^- ; (2) electron-rich Cu
32 are more conducive to the occurrence of NO_3^- reduction. The mutual confirmation of online
33 differential electrochemical mass spectrometry and density functional theory calculations
34 demonstrates that PdCu alloys block the generation of *NOH intermediate and facilitate the
35 formation of *N, finally leading to a higher catalytic performance.

36

37 **Introduction**

38 Ammonia (NH_3) has been deemed as an energy carrier for hydrogen besides as a main
39 component in chemical fertilizers.¹⁻³ Therefore, greater demand for NH_3 is foreseeable.⁴⁻⁵ The
40 industrial NH_3 synthesis through the classical Haber-Bosch process demands drastic reaction
41 conditions of high pressures (15-25 MPa) and temperatures (300-550 °C),⁶ which consumes 1-2%
42 of the world's annual energy supply.⁷⁻⁹ Considering such extremely harsh condition and fossil fuels
43 shortage, NH_3 production at atmospheric pressure and under ambient temperature is one of the
44 greatest challenges and has been pursued actively for over a century.¹⁰⁻¹²

45 As an alternative, electrocatalytic N_2 reduction at ambient conditions with proton derived from
46 decomposition of H_2O has recently attracted research interest.¹³ However, a low yield rate and a

47 low achievable selectivity at high current densities has plagued its future.¹⁴ Among all the nitrogen-
48 containing alternatives, nitrate (NO_3^-) is undoubtedly the most promising.¹⁵⁻¹⁶ The disintegration
49 of NO_3^- into the deoxygenated species only requires an energy of 204 kJ/mol, much lower than the
50 cleavage energy of $\text{N}\equiv\text{N}$ bond (941 kJ/mol).¹³⁻¹⁴ Meanwhile, higher reaction energy barrier for N_2
51 reduction occurring at solid-gas-liquid interfaces is demanded compared to that of nitrate reduction
52 reaction (NITRR) at solid-liquid interfaces.¹⁵⁻¹⁶ In view of energy consumption, exploring the
53 electrocatalytic NITRR makes perfect sense for low temperature NH_3 synthesis.¹⁷⁻²³ Currently, the
54 reduction treatment of exhaust gas NO_x (such as NO and NO_2) from the stationary sources requires
55 considerable energy since this process is conducted at high temperature ($> 400\text{ }^\circ\text{C}$).¹⁻² Our
56 approach is to convert NO_x into NO_3^- solution by oxidation and leaching absorption process and
57 subsequent effectively convert NO_3^- into value-added NH_3 .²³ Hence the technology of
58 electrocatalytic NH_3 synthesis from NO_3^- reduction is also expected to incorporated into an
59 existing technological to control NO_x emission and further obtain valuable H_2 and fertilizers
60 (Figure S1).²⁴⁻³⁰

61 With traditional metal-based catalysts, the complicated eight electrons reduction course and
62 competitive hydrogen-evolving reaction (HER) at high potentials heavily retard their selectivity
63 of NITRR.²⁷⁻³⁰ Hence designing and constructing efficient electrocatalysts with high selectivity
64 for NH_3 synthesis are necessary. Alloying presents unique strategy to tailor the geometric and
65 electronic structures of the catalyst surfaces. The coexistence of the heterogeneous metal species
66 could trigger synergistic effects that stabilize key reaction radicals or facilitate multistep reactions,
67 which could be a good candidate for NITRR.^{27,31} Among alloys, Cu alloys nanoparticles (NPs) are
68 typical and primary members.³² For instance, Sargent et al. have already reported that Ni in NiCu
69 alloys can efficiently tune the electrons property of Cu and then modulate the adsorption property

70 of intermediates ($*\text{NH}_2$, $*\text{NO}_2$, and $*\text{NO}_3^-$) in NITRR.³² However, they did not discuss whether
71 this promotion effect is feasible. By comparing the differences in other applications of NiCu and
72 PdCu alloys,¹⁵⁻¹⁶ such promotion effect should be more obvious for PdCu alloys in NITRR. PdCu
73 alloys are therefore chosen to study reaction mechanism on how the change of adsorption sites of
74 Cu alloys affects the intermediates in NITRR, which has not been unveiled.³³ In addition, the
75 research on the structure-activity relationship between Cu-based catalysts and NITRR is intriguing
76 and challenging.³¹

77 In this work, mesoporous hollow sphere Pd/Cu₂O hybrids containing highly dispersed PdCu
78 alloys and an ultrathin Cu₂O shell are proved for the first time to perform outstanding FEs
79 (94.32%), high NH₃ selectivity (96.7%), and conversion rate (99.82%) in NITRR. The quantitative
80 analysis of NH₃ is conducted by both colorimetric methods and ¹H nuclear magnetic resonance
81 (NMR) spectra. ¹⁵N isotope labeling experiments show that N in NH₃ derives from NO₃⁻. The
82 projected density of states (PDOS) of Cu_{3d} indicates that Pd species make Cu 3d orbitals easier to
83 polarize and act as new adsorption sites instead of Cu₂O. The mutual confirmation of online
84 differential electrochemical mass spectrometry (DEMS) and density functional theory (DFT)
85 calculations demonstrates that highly dispersed PdCu alloys can tune the original NH₃ synthesis
86 path of Cu₂O by changing the adsorption sites of NO₃⁻, that is, blocking the generation of $*\text{NOH}$
87 intermediate and facilitating the formation of $*\text{N}$ intermediate, ultimately leading to a higher
88 selectivity and FEs. In addition, mesoporous hollow structure of Pd/Cu₂O hybrids also contribute
89 to the efficient catalysis in NH₃ synthesis. This study opens up a new frontier for acquiring a better
90 NH₃ synthesis approach under mild conditions.

91

92 **Results**

93 **The structural characterization of Pd/Cu₂O hybrids.** The synthesis of mesoporous hollow
94 sphere Pd/Cu₂O hybrids began with the preparation of cubic Cu₂O in the presence of NaOH and
95 L-Ascorbic acid (AA) solution (Figure 1a and Figure S2c). Subsequently, a solution-processed
96 impregnation-reduction method was performed to prepare Pd/Cu₂O hybrids. Crystal facets (111)
97 of Cu₂O gradually expose instead of crystal facets (100) under the influence of
98 poly(vinylpyrrolidone) (PVP) and AA (Figure 1c). Then, partial Cu₂O and the impregnated PdCl₄²⁻
99 ions were reduced simultaneously owing to the reduction effect of AA and finally form Pd/Cu₂O
100 hybrids with dominant crystal facet (111). N₂ adsorption–desorption isotherm with H₃ hysteresis
101 loop (Figure S2a) and pore size distribution with 4 nm of average size (Figure S2b) of Pd/Cu₂O
102 hybrids show the successful preparation of mesoporous hollow sphere structure (Figure S2d-e),
103 which can efficiently promote the mass transport of electrolytes and expose more active sites of
104 inside and outside surface in NITRR. Moreover, the changes of Pd/Cu molar ratios do not affect
105 the shape and pore size distribution of Pd/Cu₂O hybrids (Figure S3) while the choices of the
106 reductant (Figure S4a), the surfactant (Figure S4b), and reaction temperature (Figure S4c) play a
107 vital role in constructing the mesoporous hollow shape.

108 The obtained sample was characterized by the high-angle annular dark-field scanning
109 transmission electron microscopy (HAADF-STEM). Pd/Cu₂O hybrids show hollow sphere with
110 ca. 300 nm of diameter (Figure 1b). Atomic-resolution HAADF-STEM images (Figure 1c) show
111 many bright dots but no obvious gathered Pd NPs distributed on Cu₂O (111) facets with the
112 corresponding lattice spacings of 2.24 Å. Further, energy dispersive spectroscopy (EDS) mapping
113 technique (high-resolution in Figure 1d and low-resolution in Figure S2f) and the corresponding
114 EDS elemental line scan (Figure 1e) confirm that highly dispersed Pd species tightly chelate with
115 partial Cu species, implying highly dispersed PdCu alloys NPs form. Simultaneously, deposition

116 of excessive Pd species on Cu₂O results in the aggregations of Pd NPs (Figure S5), which will
117 have a negative effect on NITRR (Figure S16a).

118 From X-ray diffraction patterns (XRD, Figure S6a), Pd/Cu₂O hybrids show typical diffraction
119 peaks of Cu₂O with a dominantly exposed (111) facet, which coincides well with the HAADF-
120 STEM image (Figure 1c). Meanwhile, diffraction peaks that are assignable to (111) and (220)
121 planes of metallic species situate between the corresponding Cu (JCPDS 04-0836) and Pd (JCPDS
122 46-1043) peaks and are close to PdCu (JCPDS 48-1551), confirming the formation of PdCu alloys.
123 This result is consistent with EDS-mapping analysis. X-ray photoelectron spectroscopy (XPS,
124 Figure S6b) spectra are obtained from Pd/Cu₂O hybrids and Cu₂O. In Cu 2p XPS spectra, since
125 the binding energies of Cu⁰ and Cu⁺ species are very close, two peaks (931.7 and 951.5 eV) in
126 Pd/Cu₂O hybrids are difficult to attribute to the 2p_{3/2} and 2p_{1/2} peaks of Cu⁰ or Cu⁺, respectively,
127 which shift to lower binding energies than that of Cu₂O, indicating electrons of Pd species are
128 transferred to the Cu⁺ species. Cu LMM Auger electron spectroscopy (AES) was thus performed
129 to distinguish Cu⁰ and Cu⁺ species (Figure S6c). Compared to Cu₂O, Pd/Cu₂O hybrids contain both
130 Cu⁰ (567.5 eV) and Cu⁺ (570.1 eV), which fits in with the analysis of XRD patterns. Similarly,
131 Raman spectroscopy of initial cubic Cu₂O shows four characteristic peaks of Cu₂O centered at 148,
132 218, 412, and 625 cm⁻¹ (Figure S7). Raman spectra of Pd/Cu₂O hybrids are mostly unchanged
133 relative to those of Cu₂O. Only peak positions shift to the lower wavelength compared to that of
134 Cu₂O, implying the electrons cloud transfer of Pd species to Cu⁺ and form Pd-Cu bonds.³⁴ In
135 addition, the binding energies at 340.8 and 335.6 eV for Pd 3d XPS spectrum (Figure S6d) are
136 attributed to the 3d_{3/2} and 3d_{5/2} peaks of Pd⁰, respectively. The shift of the binding energies of Cu
137 2p and Pd 3d with the increase of Pd content (Figure S8) stems from the charge transfer and
138 electronic interaction between Pd and Cu.

139 X-ray absorption fine structure (XAFS) measurements were also conducted to investigate the
140 structural parameters and coordination environments of samples. First, the X-ray absorption near-
141 edge structure (XANES) spectra indicate the line intensity of Pd/Cu₂O hybrids locates between
142 those of Cu₂O and Cu foil references (Figure 2a), suggesting that Cu⁺ ions in hybrids were partially
143 reduced to Cu⁰. Fourier transformation XAFS (FT-EXAFS) spectrum of Pd/Cu₂O shows a
144 dominant Cu-O bonds at 1.4 Å (Figure 2b). Note that this Cu–O distance is shorter than that in
145 Cu₂O, suggesting the deposited Pd also perturb the balanced state of Cu-O bonds. XANES
146 spectrum for Pd element in Pd/Cu₂O hybrids shows an intermediate strength of line compared to
147 those of Pd foil and PdO, suggesting the charge transfer from Pd to Cu⁺ (Figure 2c). The main peak
148 ascribed to Pd-Pd bonds at 2.5 Å is mainly consistent with that of Pd foil (Figure 2d), but differed
149 from those of PdO, indicating that Pd species in the hybrids exist mainly in the form of metallic
150 Pd⁰. As expected for alloys, Pd/Cu₂O hybrids show Pd-Cu bonds with distance values between
151 those for Pd and Cu (Table 1), which is also consistent with that Pd-Cu bonds at 2.4 Å in Figure
152 2b and at 2.2 Å in Figure 2d, respectively. The Cu-Cu distance is slightly reduced in Pd/Cu₂O
153 hybrids (Table 1), implying at least partial alloying of Cu and Pd atoms. These EXAFS data is
154 consistent with the XRD data, in which PdCu peaks appear.

155 **Catalytic performance of Pd/Cu₂O hybrids in NITRR.** Electrocatalytic NITRR was
156 carried out using H-type electrolytic cell (Figure S9). Catalysts loaded on carbon paper, platinum
157 foil, and Ag/AgCl (saturated KCl solution) were employed as the working, counter, and reference
158 electrodes, respectively. The anode and cathode chambers were evenly injected with 50 mL of 0.5
159 M Na₂SO₄ electrolyte (containing 100 ppm nitrate-N). Typical colorimetric methods are taken to
160 determine the concentration of NO₃⁻, nitrite (NO₂⁻), and NH₃ (Figure S10a-c). A clear difference
161 in the current density among Pd/Cu₂O hybrids, cubic Cu₂O, and commercial Cu₂O is detected by

162 linear sweep voltammetry (LSV) curves (Figure 3a). As the applied potential increases, cubic Cu₂O
163 and commercial Cu₂O (Figure S11) show relatively small current density and low onset potential
164 (0.35 V vs RHE) of NO₃⁻ reduction. On the contrary, Pd/Cu₂O hybrids present much more positive
165 onset potential (0.75 V vs RHE, pH = 9.82) than that of Cu₂O and commercial Cu₂O, indicating
166 the formed PdCu alloys promote NITRR more efficiently for NH₃ synthesis. Meanwhile, the
167 current density enhances dramatically and reaches 81.94 mA cm⁻² at -1.40 V vs RHE, which is
168 obviously higher than those of Cu₂O (53.10 mA cm⁻²) and commercial Cu₂O (43.28 mA cm⁻²).
169 Related to the effect of potential change, the FEs of NH₃ and NO₃⁻ conversion rate both reveal a
170 volcanic shape curve with maximum value (up to 94.32% for FEs and 100% for conversion rate)
171 at -0.80 V vs RHE (Figure 3b). At high potential (< -0.80 V), the FEs and conversion rate both
172 drop mainly because competing HER gradually takes place. Notably, the performance of Pd/Cu₂O
173 hybrids in electrocatalytic NITRR also surpasses other reports (Table S1). As the cathodic potential
174 was increased, the selectivity of NH₃ gradually increases and achieves stability (96.70%) from -
175 0.80 V. However, the selectivity of NO₂⁻ presents a completely opposite phenomenon (Figure S12),
176 indicating high potential facilitates NH₃ synthesis and inhibits the formation of NO₂⁻. In addition,
177 the maximum yield rate of NH₃ also obtains at -0.80 V. Thus, -0.80 V vs RHE is chosen as the
178 operation voltage. As shown in Figure 3c, the concentration of NH₃ gradually increases, whereas
179 the concentration of NO₃⁻ continuously decreases, implying the specific reduction of NO₃⁻ and the
180 formation of NH₃. Even after eight consecutive recycling tests, the FEs (around 94.32%) and NH₃
181 yield (around 0.190 mmol h⁻¹ cm⁻²) indicate no clear decay (Figure 3d). Furthermore, XRD pattern
182 (Figure S13a) and the lattice fringes of Pd/Cu₂O hybrids after long-term tests remain almost
183 unchanged (Figure S13b), confirming their potential application. Only a small peak is seen at
184 around 40 degree in XRD, indicating the slight aggregation of Pd NPs after long term use.

185 Although the conversion of NO_3^- and the selectivity of NH_3 both reveal a slight decline with the
186 increase of NO_3^- -N concentration (from 50 ppm to 400 ppm), they still remain a high and
187 competitive level percentage ($> 80\%$) (Figure 3e), indicating the excellent performance of
188 Pd/Cu₂O hybrids. To highlight the effect of PdCu alloys, reference catalysts (Cu₂O and commercial
189 Cu₂O) were studied in NITRR under the same conditions. As shown in Figure 3f, the NH_3
190 selectivity (96.70%), conversion rate of NO_3^- (99.82%), and FEs (94.32%) of Pd/Cu₂O hybrids are
191 obvious higher than those of Cu₂O (68.71%, 70.58%, 60.36%) and commercial Cu₂O (58.74%,
192 55.39%, and 49.88%), indicating PdCu alloys play an important part in improving the overall
193 catalytic activity. Meanwhile, compared to Cu₂O and commercial Cu₂O, Pd/Cu₂O hybrids show
194 the highest yield rate of NH_3 (Figure S14a) and lowest yield of NO_2^- (Figure S14b). The above
195 analysis ascertains that PdCu alloys are important in decreasing the overpotential and improving
196 the NH_3 selectivity, conversion rate of NO_3^- , and FEs of Pd/Cu₂O hybrids (for potential-dependent
197 catalytic performances of Cu₂O and commercial Cu₂O, see Figure S15). Furthermore, with the
198 variation of molar percentage of Pd/Cu, Pd(2 mol%)Cu/Cu₂O hybrids achieve the highest
199 performance in NITRR (Figure S16a), it is mainly due to the low deposition of Pd⁰ at low Pd
200 content and the aggregation of Pd NPs at high content, respectively. To highlight the structure-
201 activity relationship between Pd/Cu₂O hybrids and NH_3 synthesis, Pd/Cu₂O hybrids without
202 mesoporous hollow structure were also prepared by changing the reductant, surfactant, and
203 synthesis temperature, respectively, which all showed considerably lower activity than that of
204 Pd/Cu₂O hybrids with mesoporous hollow structure (Figure S16b). Hence Pd/Cu₂O hybrids with
205 suitable molar ratio of Pd/Cu and mesoporous hollow sphere structure show incomparable
206 superiority in NH_3 synthesis.

207 **¹H NMR spectra.** The comparison test was performed in blank Na₂SO₄ solution to eliminate

208 the possible distractions from external environment and electrocatalyst itself (Figure 4a). The
209 result indicates almost negligible NH₃ generation, ascertaining nitrogen species in NH₃ derive
210 entirely from NO₃⁻. Furthermore, by ¹H nuclear magnetic resonance (NMR), ¹⁵N isotope labeling
211 experiments were carried out to verify the sources of NH₃. Adopting Na¹⁴NO₃ as reactants, the ¹H
212 NMR (600 MHz) spectra of electrolyte show typical triple peaks of ¹⁴NH₄⁺. On the contrary, when
213 the electrocatalytic reduction of Na¹⁵NO₃ is performed, the ¹H NMR spectra of electrolyte indicate
214 typical double peaks of ¹⁵NH₄⁺ at $\delta = 7.07$ and 6.95 ppm (Figure 4b), again revealing that NH₃ is
215 completely derived from the electroreduction of NO₃⁻. In light of the positive correlation between
216 NH₃ content and peak area of ¹H NMR, ¹H NMR with external standard (maleic acid, C₄H₄O₄)
217 can further quantify the concentration of NH₄⁺ (Figure S17). Based on the standard curve of the
218 integral area against ammonium concentration (Figure S17c-d), similar yields of ¹⁴NH₄⁺-¹⁴N and
219 ¹⁵NH₄⁺-¹⁵N were achieved. The quantitative results of ¹H NMR perfectly correspond to that of
220 colorimetric methods using Nessler's reagent (Table S2), confirming the accuracy of different
221 quantitative methods for quantifying ammonia. By the electrochemical double layer capacitances,
222 the electrochemical active surface areas (ECSA) are evaluated to shed light on the origin of high
223 activity of Pd/Cu₂O hybrids. Interestingly, although the ECSA of Pd/Cu₂O hybrids (10.1 cm²) was
224 slightly lower than that of Cu₂O (14.2 cm²), the LSV curve of Pd/Cu₂O hybrids still has a stronger
225 current density than that of Cu₂O (Figure S18) after normalization to the ECSA, indicating a higher
226 intrinsic performance of Pd/Cu₂O hybrids with the assistance of PdCu alloys.

227 **Online DEMS and DFT calculations.** To reveal the origin of the adsorption sites variation
228 of NO₃⁻ and understand the electronic properties of Pd/Cu₂O hybrids, we systematically studied
229 the electronic structures of Pd/Cu₂O hybrids and Cu₂O by the projected density of states (PDOS)
230 of Cu 3d orbitals (Figure 5a-b). As compared to Cu₂O that has semiconductor-like band structure,

231 Pd/Cu₂O hybrids show metallic feature with continuous valence band across the Fermi level into
232 the conduction band (CB).³¹ That is, the deposition of Pd makes the band gap of Cu 3d disappear,
233 realizing the transition from semiconductor to conductor. Electrons transfer from the coordinating
234 Pd 3d orbitals to the Cu 3d orbitals takes place, thereby leading to partial reduction of Cu⁺ and
235 forming Pd–Cu bonds; this is in good line with XRD, XPS, and XAFS experimental results.
236 Electrons transfer (Pd 3d → Cu 3d orbitals) makes NO₃⁻ negative ions more tend to adsorb on Pd
237 species, which results in a decrease in adsorption energy.³¹ Compared with symmetric spins of Cu
238 3d orbitals in pure Cu₂O, the asymmetric spin orbitals of Cu 3d in Pd/Cu₂O hybrids above Fermi
239 level indicate that Pd induces Cu 3d orbitals from the original non-polarization to polarization by
240 Pd perturbation.^{31, 35} Subsequently, Cu atoms transfer charges to adjacent O atoms, leading to new
241 intermediate state at the Fermi level (Figure S19). The CB of O 2p orbitals moves towards Fermi
242 level, which indicates that the delocalization of O 2p electrons is enhanced and localization is
243 weakened. Furthermore, online differential electrochemical mass spectrometry (DEMS) is adopted
244 for detecting the molecular intermediates and products over Pd/Cu₂O hybrids and Cu₂O. During
245 continuous four cycles, the m/z signals of 17, 33, 30, 46 that attribute to NH₃, NH₂OH, NO, and
246 NO₂, respectively, appeared by changing the applied voltage from 0.78 to -1.42 V. Under the same
247 voltage range, intermediate NH₂OH that obviously appears over Cu₂O is almost completely
248 suppressed over Pd/Cu₂O hybrids (Figure 5c-d), suggesting Pd/Cu₂O hybrids and Cu₂O follow
249 different reaction pathways in NITRR. According to the results of DEMS, we can deduce the
250 reaction pathways in NITRR and calculate free energy of every intermediate over Pd/Cu₂O hybrids
251 and Cu₂O (Figure 5e-f). The stable structural models used in this work are shown in the Supporting
252 Information (Figure S20). It is worth noting that the adsorption sites of NO₃⁻ on Cu₂O (Cu species
253 as adsorption sites) are replaced by Pd species of Pd/Cu₂O hybrids. Adsorption energy (0.63 eV)

254 of NO_3^- on Pd/Cu₂O hybrids is slightly lower than that (0.70 eV) of Cu₂O, mainly due to the
255 transformation of adsorption sites, implying PdCu alloys can facilitate the adsorption of NO_3^- to
256 form *NO₃. Subsequently, for both Pd/Cu₂O hybrids and Cu₂O, *NO₂ and *NO species are
257 gradually generated by the continuous cleavage of N-O bond of *NO₃. Then, from *NO species,
258 the reaction paths in NITRR diverge. One is the deoxidization process of *NO and the other is the
259 hydrogenation process of *NO (Figure S21). The deoxidization process of *NO to *N species over
260 Pd/Cu₂O hybrids only needs 0.53 eV, far less than 1.62 eV for Cu₂O. On the contrary, the
261 hydrogenation process of *NO to *NOH species over Pd/Cu₂O hybrids needs 0.91 eV, which is
262 higher than 0.38 eV for Cu₂O. Furthermore, 1.62 eV (*NO to *N) for Cu₂O and 0.91 eV (*NO to
263 *NOH) for Pd/Cu₂O are also higher than the adsorption energy (0.63 eV) of NO_3^- on Pd/Cu₂O
264 hybrids and (0.70 eV) on Cu₂O, respectively. Based on DEMS analysis and DFT calculations
265 results, Pd/Cu₂O hybrids prefer to perform the deoxidization process of *NO while Cu₂O tends to
266 perform the hydrogenation process (Figure 5e-f). Starting from *N species, hydrogenation process
267 occurs as follows, *N → *NH → *NH₂ → *NH₃, according to a previous report.¹⁷ As for *NOH
268 species, hydrogenation process is also followed, *NOH → *NH₂OH → *NH₃. In view of the
269 performance of NITRR over Pd/Cu₂O hybrids and Cu₂O, we can deduce that the formed PdCu
270 alloys restrain the formation of *NOH intermediates and promote the formation of *N
271 intermediates, eventually resulting in a higher selectivity and Faradaic efficiency.

272

273 **Conclusion**

274 In summary, we investigated the relationship between intermediates and performance of
275 NITRR on Pd/Cu₂O hybrids with mesoporous hollow sphere structure. By depositing Pd species
276 on Cu₂O, we achieved significantly improved NH₃ synthesis performance. Pd species make Cu 3d

277 orbitals easier to polarize and act as new adsorption sites instead of Cu₂O. The mutual confirmation
278 of online DEMS and DFT calculations demonstrates that highly dispersed PdCu alloys formed by
279 the deposition of Pd⁰ on Cu₂O can tune the original ammonia synthesis path of Cu₂O by changing
280 the adsorption sites of NO₃⁻, that is, blocking the generation of *NOH intermediate and facilitating
281 the formation of *N intermediate, ultimately leading to a higher selectivity and Faradaic efficiency.
282 In addition, mesoporous hollow structure of Pd/Cu₂O hybrids also contribute to the efficient
283 catalysis in NH₃ synthesis. This work highlights a promising route to design alloying catalysts for
284 selective electrocatalytic NO₃⁻ reduction to NH₃.

285 **Methods**

286 **Synthesis of Cu₂O**

287 All of the chemical reagents used in this experiment were of analytical grade and used without
288 further purification. In a typical synthesis, 1 mmol CuCl₂·2H₂O was dissolved into the 100 mL of
289 aqueous solution. Then, 10.0 mL NaOH aqueous solution (2.0 mol L⁻¹) was added dropwise into
290 the above transparent light green solution. During the process, the solution color turned into turbid
291 blue-green, and then dark brown. After stirring for 0.5 h, L-Ascorbic acid solution (10.0 mL, 0.6
292 M) was added dropwise into the dark brown solution. A turbid red liquid gradually formed. The
293 mixture was aged for 3 h. All of procedures were carried out under constant stirring and heated in
294 a water bath at a given temperature (80 °C). The resulting precipitate was collected by
295 centrifugation, followed by washing with distilled water 3 times and absolute ethanol twice to
296 remove the residual inorganic ions and polymer, and finally dried in vacuum at 60 °C for 5 h for
297 further characterization.

298 **Synthesis of Pd/Cu₂O hybrids with mesoporous hollow sphere structure**

299 In a typical synthesis, 40 mg of Cu₂O cubes was dispersed in 8 mL of an aqueous solution. Then

300 105 mg of polyvinylpyrrolidone K-30 (PVP), 120 mg of L-Ascorbic acid were added into the glass
301 vial under magnetic stirring in an oil bath preset to 80 °C for 10 min. Subsequently, a certain
302 amount of K_2PdCl_4 solution was injected into the reaction solution. The reaction mixture was
303 heated at 80 °C in air for 3h. The samples were washed with water several times to remove most
304 of PVP and L-Ascorbic acid by centrifugation. The obtained samples were denoted as Pd(0.5
305 mol%)/Cu₂O, Pd(1 mol%)/Cu₂O, Pd(2 mol%)/Cu₂O (or Pd/Cu₂O), Pd(3.0 mol%)/Cu₂O, and
306 Pd(4.0 mol%)/Cu₂O, respectively, according to the amount of added K_2PdCl_4 and Cu₂O. For
307 comparison, Pd/Cu₂O hybrids without PVP, with NaBH₄ instead of L-Ascorbic acid, and 50 °C of
308 reaction temperature instead of 80 °C were also synthesized in the same manner, respectively.

309 **Material characterization**

310 The X-ray diffraction (XRD) patterns were recorded using a BRUKER D8/Advance X-ray
311 diffractometer (Cu K α X-ray: $\lambda = 0.1545$ nm). The scanning electron microscopy (SEM) images
312 were taken on a ZEISS GEMINISEM 500 electron field emission microscope. Transmission
313 electron microscopy (TEM) and energy-dispersive spectroscopy (EDS) measurements were
314 performed on a JEOL JEM 2100 microscope with an accelerating voltage of 200 kV. X-ray
315 photoelectron spectroscopy (XPS) and Auger electron spectroscopy measurements were carried
316 out using an ESCALab250XI photoelectron spectrometer. All binding energies were referenced to
317 the C 1s peak at 284.8 eV. The pore size distribution and specific surface area were calculated
318 according to Barrett-Joyner-Halenda (BJH) and Brunauer-Emmett-Teller (BET) methods based on
319 N₂ adsorption isotherms measured at -196 °C on MicrotracBEL Corp. Samples were degassed
320 under vacuum at 200 °C for 4 h prior to data collection. Raman spectroscopy was tested on
321 Confocal Raman microscope under an excitation of 532 nm laser light. Cu *K*-edge and Pd *K*-edge
322 XAFS measurements were performed on the beamline BL01C1 in NSRRC. The radiation was

323 monochromatized by a Si (111) double-crystal monochromator. The ultraviolet-visible (UV-Vis)
324 absorbance spectra were measured on Lambda 900 from PerkinElmer UV WinLab. The isotope
325 labeling experiments were measured by ^1H -NMR measurement (Bruker 600-MHz system). The
326 differential electrochemical mass spectrometry (DEMS, HPR-400) was provided by ExtraTech
327 Analytical Limited to perform online analysis of produced intermediates and products.

328 **Electrochemical measurements**

329 The electrochemical measurements were carried out using a CH Instruments, CHI760E
330 electrochemical workstation (Chenhua, Shanghai) in an H-type electrolytic cell separated by a
331 membrane. The copper-based sample on carbon paper, saturated Ag/AgCl electrode and platinum
332 foil were used as the working electrode, reference electrode and counter electrode, respectively.
333 The surface area of the working electrode was controlled with 1 cm^2 . $0.5\text{ M Na}_2\text{SO}_4$ solution (100
334 mL) was evenly distributed to the cathode and anode compartment. NaNO_3 was added into the
335 cathode compartment for NO_3^- reduction (containing 100 ppm nitrate-N). All potentials were
336 recorded against the reversible hydrogen electrode (RHE). Before nitrate electroreduction test,
337 linear sweep voltammetry (LSV) curves are performed until that the polarization curves achieve
338 steady-state ones at a rate of 10 mV s^{-1} from 0.78 to -1.42 V. Then, the potentiostatic test was
339 carried out at different potentials for 1.5 h with a stirring rate of 300 rpm. Cyclic voltammetry (CV)
340 curves in electrochemical double-layer capacitance (C_{dl}) determination were measured in a
341 potential window nearly without the Faradaic process at different scan rates of 10, 20, 40, 60, 80,
342 and 100 mV s^{-1} . The plot of current density at set potential against scan rate has a linear relationship
343 and its slope is the C_{dl} .

344 **Online DEMS measurements**

345 1000 ppm NO_3^- -N with $0.5\text{ M Na}_2\text{SO}_4$ electrolyte was kept flowing into a specially-made

346 electrochemical cell through a peristaltic pump. Ar was bubbled into the electrolyte constantly
347 before and during the DEMS measurements. Carbon paper coated with Pd/Cu₂O electrocatalysts,
348 Pt wire, and saturated Ag/AgCl electrode were used as the working electrode, the counter electrode
349 and the reference electrode, respectively. LSV technology was employed from 0.78 to -1.42 V at
350 a scan rate of 10 mV s⁻¹ until the baseline kept steady. Then, the corresponding mass signals
351 appeared. After the electrochemical test was over and the mass signal returned to baseline, the next
352 cycle was started using the same test conditions to avoid the accidental error during DEMS
353 measurements. After four cycles, the experiment was ended.

354 **Determination of ion concentration**

355 The ultraviolet-visible (UV-Vis) spectrophotometer was used to detect the ion concentration
356 of pre- and post-test electrolytes after diluting to appropriate concentration to match the range of
357 calibration curves. The specific detection methods are as follow:

358 Determination of nitrate-N:

359 Firstly, a certain amount of electrolyte was taken out from the electrolytic cell and diluted to
360 5 mL to detection range. Then, 0.1 mL 1 M HCl and 0.01 mL 0.8 wt% sulfamic acid solution were
361 added into the aforementioned solution. The absorption spectrum was measured using an
362 ultraviolet-visible spectrophotometer and the absorption intensities at a wavelength of 220 nm and
363 275 nm were recorded. The final absorbance value was calculated by this equation: $A = A_{220\text{nm}} -$
364 $2A_{275\text{nm}}$. The concentration-absorbance curve was calibrated using a series of standard potassium
365 nitrate solutions and the potassium nitrate crystal was dried at 105 - 110 °C for 2 h in advance.

366 Determination of nitrite-N

367 A mixture of *p*-aminobenzenesulfonamide (4 g), N-(1-Naphthyl) ethylenediamine
368 dihydrochloride (0.2 g), ultrapure water (50 mL) and phosphoric acid (10 mL, $\rho = 1.70$ g/mL) was

369 used as a color reagent. A certain amount of electrolyte was taken out from the electrolytic cell and
370 diluted to 5 mL to detection range. Next, 0.1 mL color reagent was added into the aforementioned
371 5 mL solution and mixed uniformly, and the absorption intensity at a wavelength of 540 nm was
372 recorded after sitting for 20 min. The concentration-absorbance curve was calibrated using a series
373 of standard sodium nitrite solutions.

374 **Determination of ammonia-N:**

375 Ammonia-N was determined using Nessler's reagent as the color reagent. First, a certain
376 amount of electrolyte was taken out from the electrolytic cell and diluted to 5 mL to detection
377 range. Next, 0.1 mL potassium sodium tartrate solution ($\rho = 500 \text{ g/L}$) was added and mixed
378 thoroughly, then 0.1 mL Nessler's reagent was put into the solution. The absorption intensity at a
379 wavelength of 420 nm was recorded after sitting for 20 min. The concentration-absorbance curve
380 was calibrated using a series of standard ammonium chloride solutions and the ammonium chloride
381 crystal was dried at $105 \text{ }^\circ\text{C}$ for 2 h in advance.

382 **Isotope labeling experiments**

383 99.21% $\text{Na}^{15}\text{NO}_3$ was used as the feeding N-source to perform the isotopic labeling nitrate
384 reduction experiments to clarify the source of ammonia. 0.5 M Na_2SO_4 was used as electrolyte and
385 $\text{Na}^{15}\text{NO}_3$ with a concentration of 100 ppm $^{15}\text{NO}_3^-$ - ^{15}N was taken out and the pH value was adjusted
386 to be weak acid with 4 M H_2SO_4 for further quantification by ^1H NMR (600 MHz) with external
387 standards of maleic acid. The calibration curve was created as follows: First, a series of $^{15}\text{NH}_4^+$ -
388 ^{15}N solutions ($(^{15}\text{NH}_4)_2\text{SO}_4$) with known concentration (50, 100, 150, 200, 250 ppm) were
389 prepared in 0.5 M Na_2SO_4 as standards; Second, 50 mL of the $^{15}\text{NH}_4^+$ - ^{15}N standard solution with
390 different concentration was mixed with 0.02 g maleic acid; Third, 50 μL deuterium oxide (D_2O)
391 was added in 0.5 mL above mixed solution for the NMR detection; Fourth, the calibration was

392 achieved using the peak area ratio between $^{15}\text{NH}_4^+$ - ^{15}N and maleic acid because the $^{15}\text{NH}_4^+$ - ^{15}N
393 concentration and area ratio were positively correlated. Similarly, the amount of $^{14}\text{NH}_4^+$ - ^{14}N was
394 quantified by this method when $\text{Na}^{14}\text{NO}_3$ was used as the feeding N-source.

395 **Calculation of the yield, conversion rate, selectivity, and Faradaic efficiency.**

396 For nitrate electroreduction, the yield was calculated by the Eq. 1:

$$397 \quad \text{Yield}_{\text{NH}_3} = (c_{\text{NH}_3} \times V) / (M_{\text{NH}_3} \times t \times S) \quad (1)$$

398 The conversion rate can be calculated as follows:

$$399 \quad \text{Conversion} = \Delta c_{\text{NO}_3^-} / c_0 \times 100\% \quad (2)$$

400 The selectivity of ammonia and nitrate were obtained by the Eq. 3:

$$401 \quad \text{Selectivity} = c / \Delta c_{\text{NO}_3^-} \times 100\% \quad (3)$$

402 The Faradaic efficiency was defined from the electric charge consumed for synthesizing ammonia
403 and total charge passed through the electrode according to Eq. 4:

$$404 \quad \text{Faradaic efficiency} = (8F \times c_{\text{NH}_3} \times V) / (M_{\text{NH}_3} \times Q) \quad (4)$$

405 Where c_{NH_3} is the mass concentration of $\text{NH}_3(\text{aq})$, V is the volume of electrolyte in the cathode
406 compartment (50 mL), M_{NH_3} is the molar mass of NH_3 , t is the electrolysis time (2 h), S is the
407 geometric area of working electrode (1 cm^2), $\Delta c_{\text{NO}_3^-}$ is the concentration difference of NO_3^- before
408 and after electrolysis, c_0 is the initial concentration of NO_3^- , c is the generated concentration of
409 ammonia or nitrite, F is the Faradaic constant (96485 C mol^{-1}), Q is the total charge passing the
410 electrode.

411 **DFT calculation detail**

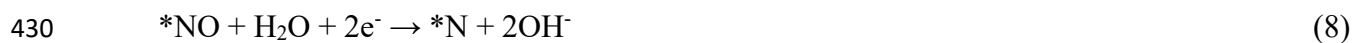
412 The Vienna ab initio simulation package (VASP, version 5.4.4) was utilized to calculate the
413 properties of Pd/ Cu_2O hybrids and Cu_2O . All of the model structures were optimized by using the
414 Perdew-Burke-Ernzerhof (PBE) form of the generalized gradient approximation plus the Hubbard

415 model (GGA+U), with a 400 eV of kinetic cutoff energy. The U_{eff} (i.e., $U-J$) of Cu in this study
416 was set at 7.0 eV.³⁶

417 As presented in TEM images and XRD patterns, crystal facets (111) of Cu_2O in Pd/ Cu_2O
418 hybrids were dominantly exposed. Therefore, the (111) surface of Cu_2O , as the most stable surface,
419 was chosen to be reconstructed as the slab model, featuring a $[3\times 3]$ supercell and three Cu_2O
420 layers.¹³ The slab model of PdCu was constructed by loading a triatomic cluster of Pd on the Cu_2O
421 (111) surface. Thus, the atomic ratio of Pd to Cu was close to that of XPS results. These slab
422 models were separated by a 15 Å vacuum combined with a $1\times 1\times 1$ Gamma-Pack k-point mesh due
423 to the large crystal cell ($\sim 18 \text{ Å}\times 18 \text{ Å}$) of slab model. Moreover, all of the slab models were relaxed
424 until the SCF tolerance was below 10^{-6} eV and atomic forces were below 0.05 eV/Å.

425 The reaction energy of each elementary reaction was calculated based on these equations:

426 Path 1



434 Path 2





441

442 **Data availability**

443 The data within the article and Supplementary Information of the current study are available from
444 the authors upon reasonable request.

445

446 **References**

447 1. Erisman, J. W.; Sutton, M. A.; Galloway, J.; Klimont, Z.; Winiwarter, W., How a century of ammonia
448 synthesis changed the world. *Nat. Geosci.* **2008**, *1* (10), 636-639.

449 2. Ye, T. N.; Park, S. W.; Lu, Y. F.; Li, J.; Sasase, M.; Kitano, M.; Tada, T.; Hosono, H., Vacancy-enabled N₂
450 activation for ammonia synthesis on an Ni-loaded catalyst. *Nature* **2020**, *583* (7816), 391-395.

451 3. Wang, D.; Peng, Y.; Yang, Q.; Xiong, S.; Li, J.; Crittenden, J., Performance of modified La_xSr_{1-x}MnO₃
452 perovskite catalysts for NH₃ oxidation: TPD, DFT, and kinetic studies. *Environ. Sci. Technol.* **2018**, *52* (13), 7443-
453 7449.

454 4. Pool, J. A.; Lobkovsky, E.; Chirik, P. J., Hydrogenation and cleavage of dinitrogen to ammonia with a
455 zirconium complex. *Nature* **2004**, *427* (6974), 527-530.

456 5. Zhu, D.; Zhang, L.; Ruther, R. E.; Hamers, R. J., Photo-illuminated diamond as a solid-state source of
457 solvated electrons in water for nitrogen reduction. *Nat. Mater.* **2013**, *12* (9), 836-841.

458 6. Schlogl, R., Catalytic synthesis of ammonia-a "never-ending story"? *Angew. Chem. Int. Ed.* **2003**, *42* (18),
459 2004-2008.

460 7. Smil, V., Detonator of the population explosion. *Nature* **1999**, *400* (6743), 415-415.

461 8. Liu, Z.; Wakihara, T.; Oshima, K.; Nishioka, D.; Hotta, Y.; Elangovan, S. P.; Yanaba, Y.; Yoshikawa, T.;
462 Chaikittisilp, W.; Matsuo, T.; Takewaki, T.; Okubo, T., Widening synthesis bottlenecks: realization of ultrafast and
463 continuous-flow synthesis of high-silica zeolite SSZ-13 for NO_x removal. *Angew. Chem. Int. Ed.* **2015**, *54* (19), 5683-

- 464 5687.
- 465 9. Shima, T.; Hu, S. W.; Luo, G.; Kang, X. H.; Luo, Y.; Hou, Z. M., Dinitrogen cleavage and hydrogenation by
466 a trinuclear titanium polyhydride complex. *Science* **2013**, *340* (6140), 1549-1552.
- 467 10. Schrauzer, G. N.; Guth, T. D., Photolysis of water and photoreduction of nitrogen on titanium dioxide. *J. Am.*
468 *Chem. Soc.* **1977**, *99* (22), 7189-7193.
- 469 11. Buscagan, T. M.; Oyala, P. H.; Peters, J. C., N₂ -to-NH₃ conversion by a triphos-iron catalyst and enhanced
470 turnover under photolysis. *Angew. Chem. Int. Ed.* **2017**, *56* (24), 6921-6926.
- 471 12. Li, H.; Shang, J.; Ai, Z.; Zhang, L., Efficient visible light nitrogen fixation with BiOBr nanosheets of oxygen
472 vacancies on the exposed {001} facets. *J. Am. Chem. Soc.* **2015**, *137* (19), 6393-6399.
- 473 13. Wang, Y.; Zhou, W.; Jia, R.; Yu, Y.; Zhang, B., Unveiling the activity origin of a copper-based electrocatalyst
474 for selective nitrate reduction to ammonia. *Angew. Chem. Int. Ed.* **2020**, *59* (13), 5350-5354.
- 475 14. Chen, G. F.; Yuan, Y. F.; Jiang, H. F.; Ren, S. Y.; Ding, L. X.; Ma, L.; Wu, T. P.; Lu, J.; Wang, H. H.,
476 Electrochemical reduction of nitrate to ammonia via direct eight-electron transfer using a copper-molecular solid
477 catalyst. *Nat. Energy* **2020**, *5* (8), 605-613.
- 478 15. Gayen, P.; Spataro, J.; Avasarala, S.; Ali, A. M.; Cerrato, J. M.; Chaplin, B. P., Electrocatalytic reduction of
479 nitrate using magneli phase TiO₂ reactive electrochemical membranes doped with Pd-based catalysts. *Environ. Sci.*
480 *Technol.* **2018**, *52* (16), 9370-9379.
- 481 16. Shuai, D.; Choe, J. K.; Shapley, J. R.; Werth, C. J., Enhanced activity and selectivity of carbon nanofiber
482 supported Pd catalysts for nitrite reduction. *Environ. Sci. Technol.* **2012**, *46* (5), 2847-2855.
- 483 17. Wang, Y.; Xu, A.; Wang, Z.; Huang, L.; Li, J.; Li, F.; Wicks, J.; Luo, M.; Nam, D. H.; Tan, C. S.; Ding, Y.;
484 Wu, J.; Lum, Y.; Dinh, C. T.; Sinton, D.; Zheng, G.; Sargent, E. H., Enhanced nitrate-to-ammonia activity on copper-
485 nickel alloys via tuning of intermediate adsorption. *J. Am. Chem. Soc.* **2020**, *142* (12), 5702-5708.
- 486 18. Jung, S.; Bae, S.; Lee, W., Development of Pd-Cu/hematite catalyst for selective nitrate reduction. *Environ.*
487 *Sci. Technol.* **2014**, *48* (16), 9651-9658.
- 488 19. Chen, C.; Li, K.; Li, C.; Sun, T.; Jia, J., Combination of Pd-Cu catalysis and electrolytic H₂ evolution for
489 selective nitrate reduction using protonated polypyrrole as a cathode. *Environ. Sci. Technol.* **2019**, *53* (23), 13868-
490 13877.
- 491 20. Hansen, H. C. B.; Koch, C. B.; Nancke-Krogh, H.; Borggaard, O. K.; Sørensen, J., Abiotic nitrate reduction

492 to ammonium: Key role of green rust. *Environ. Sci. Technol.* **1996**, *30* (6), 2053-2056.

493 21. McEnaney, J. M.; Blair, S. J.; Nielander, A. C.; Schwalbe, J. A.; Koshy, D. M.; Cargnello, M.; Jaramillo, T.
494 F., Electrolyte engineering for efficient electrochemical nitrate reduction to ammonia on a titanium electrode. *ACS*
495 *Sustain. Chem. Eng.* **2020**, *8* (7), 2672-2681.

496 22. Duca, M.; Koper, M. T. M., Powering denitrification: The perspectives of electrocatalytic nitrate reduction.
497 *Environ. Sci. Technol.* **2012**, *5* (12), 9726.

498 23. Wei, L.; Liu, D.-J.; Rosales, B. A.; Evans, J. W.; Vela, J., Mild and selective hydrogenation of nitrate to
499 ammonia in the absence of noble metals. *ACS Catal.* **2020**, *10* (6), 3618-3628.

500 24. Butcher, D. P.; Gewirth, A. A., Nitrate reduction pathways on Cu single crystal surfaces: Effect of oxide and
501 Cl⁻. *Nano Energy* **2016**, *29*, 457-465.

502 25. Su, L.; Han, D.; Zhu, G.; Xu, H.; Luo, W.; Wang, L.; Jiang, W.; Dong, A.; Yang, J., Tailoring the assembly of
503 iron nanoparticles in carbon microspheres toward high-performance electrocatalytic denitrification. *Nano Lett.* **2019**,
504 *19* (8), 5423-5430.

505 26. Yamauchi, M.; Abe, R.; Tsukuda, T.; Kato, K.; Takata, M., Highly selective ammonia synthesis from nitrate
506 with photocatalytically generated hydrogen on CuPd/TiO₂. *J. Am. Chem. Soc.* **2011**, *133* (5), 1150-1152.

507 27. Li, J.; Zhan, G.; Yang, J.; Quan, F.; Mao, C.; Liu, Y.; Wang, B.; Lei, F.; Li, L.; Chan, A. W. M.; Xu, L.; Shi,
508 Y.; Du, Y.; Hao, W.; Wong, P. K.; Wang, J.; Dou, S. X.; Zhang, L.; Yu, J. C., Efficient ammonia electrosynthesis from
509 nitrate on strained ruthenium nanoclusters. *J. Am. Chem. Soc.* **2020**, *142* (15), 7036-7046.

510 28. Arikawa, Y.; Otsubo, Y.; Fujino, H.; Horiuchi, S.; Sakuda, E.; Umakoshi, K., Nitrite reduction cycle on a
511 dinuclear ruthenium complex producing ammonia. *J. Am. Chem. Soc.* **2018**, *140* (2), 842-847.

512 29. Stamenkovic, V. R.; Fowler, B.; Mun, B. S.; Wang, G. F.; Ross, P. N.; Lucas, C. A.; Markovic, N. M.,
513 Improved oxygen reduction activity on Pt₃Ni(111) via increased surface site availability. *Science* **2007**, *315* (5811),
514 493-497.

515 30. Gao, J.; Jiang, B.; Ni, C.; Qi, Y.; Bi, X., Enhanced reduction of nitrate by noble metal-free electrocatalysis
516 on P doped three-dimensional Co₃O₄ cathode: Mechanism exploration from both experimental and DFT studies. *Chem.*
517 *Eng. J.* **2020**, *382*, 123034.

518 31. Hsieh, H. H.; Chang, Y. K.; Pong, W. F.; Pieh, J. Y.; Tseng, P. K.; Sham, T. K.; Coulthard, I.; Naftel, S. J.;
519 Lee, J. F.; Chung, S. C.; Tsang, K. L., Electronic structure of Ni-Cu alloys: The d-electron charge distribution. *Phys.*

520 *Rev. B* **1998**, *57* (24), 15204-15210.

521 32. Comisso, N.; Cattarin, S.; Fiameni, S.; Gerbasi, R.; Mattarozzi, L.; Musiani, M.; Vázquez-Gómez, L.; Verlato,
522 E., Electrodeposition of Cu–Rh alloys and their use as cathodes for nitrate reduction. *Electrochim. Acta* **2012**, *25*, 91-
523 93.

524 33. Ma, S.; Sadakiyo, M.; Heima, M.; Luo, R.; Haasch, R. T.; Gold, J. I.; Yamauchi, M.; Kenis, P. J. A.,
525 Electroreduction of carbon dioxide to hydrocarbons using bimetallic Cu-Pd catalysts with different mixing patterns.
526 *J. Am. Chem. Soc.* **2017**, *139* (1), 47-50.

527 34. Chen, C.; Zhu, X. R.; Wen, X. J.; Zhou, Y. Y.; Zhou, L.; Li, H.; Tao, L.; Li, Q. L.; Du, S. Q.; Liu, T. T.; Yan,
528 D. F.; Xie, C.; Zou, Y. Q.; Wang, Y. Y.; Chen, R.; Huo, J.; Li, Y. F.; Cheng, J.; Su, H.; Zhao, X.; Cheng, W. R.; Liu, Q.
529 H.; Lin, H. Z.; Luo, J.; Chen, J.; Dong, M. D.; Cheng, K.; Li, C. G.; Wang, S. Y., Coupling N₂ and CO₂ in H₂O to
530 synthesize urea under ambient conditions. *Nat. Chem.* **2020**, *12* (8), 10.

531 35. Mattei, G.; Maurizio, C.; Mazzoldi, P.; D’Acapito, F.; Battaglin, G.; Cattaruzza, E.; de Julián Fernández, C.;
532 Sada, C., Dynamics of compositional evolution of Pd-Cu alloy nanoclusters upon heating in selected atmospheres.
533 *Phys. Rev. B* **2005**, *71* (19), 195418.

534 36. Xiong, S.; Chen, J.; Huang, N.; Yang, S.; Peng, Y.; Li, J., Balance between reducibility and N₂O adsorption
535 capacity for the N₂O decomposition: Cu_xCo_y catalysts as an example. *Environ. Sci. Technol.* **2019**, *53* (17), 10379-
536 10386.

537

538

539

540

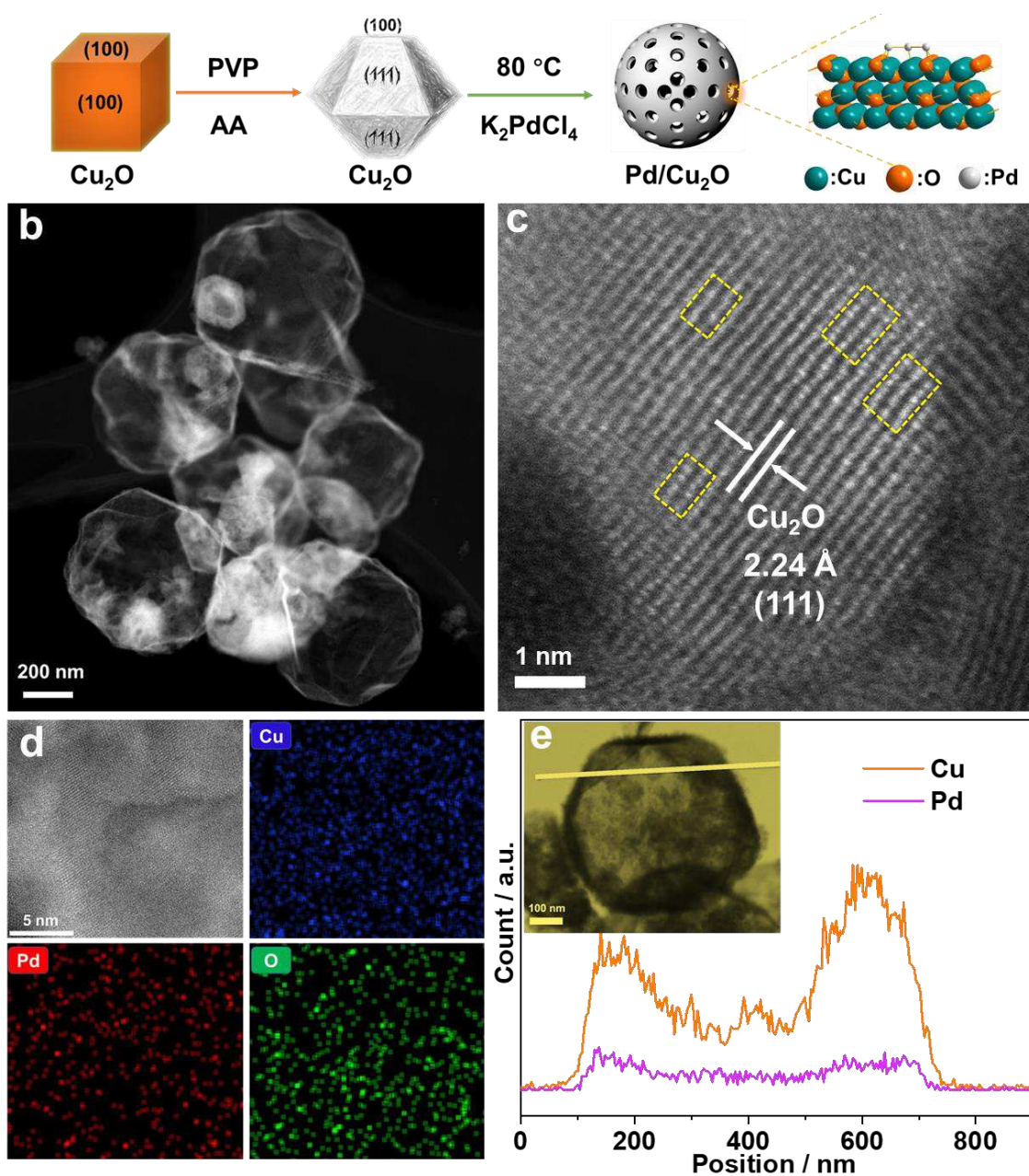
541

542

543

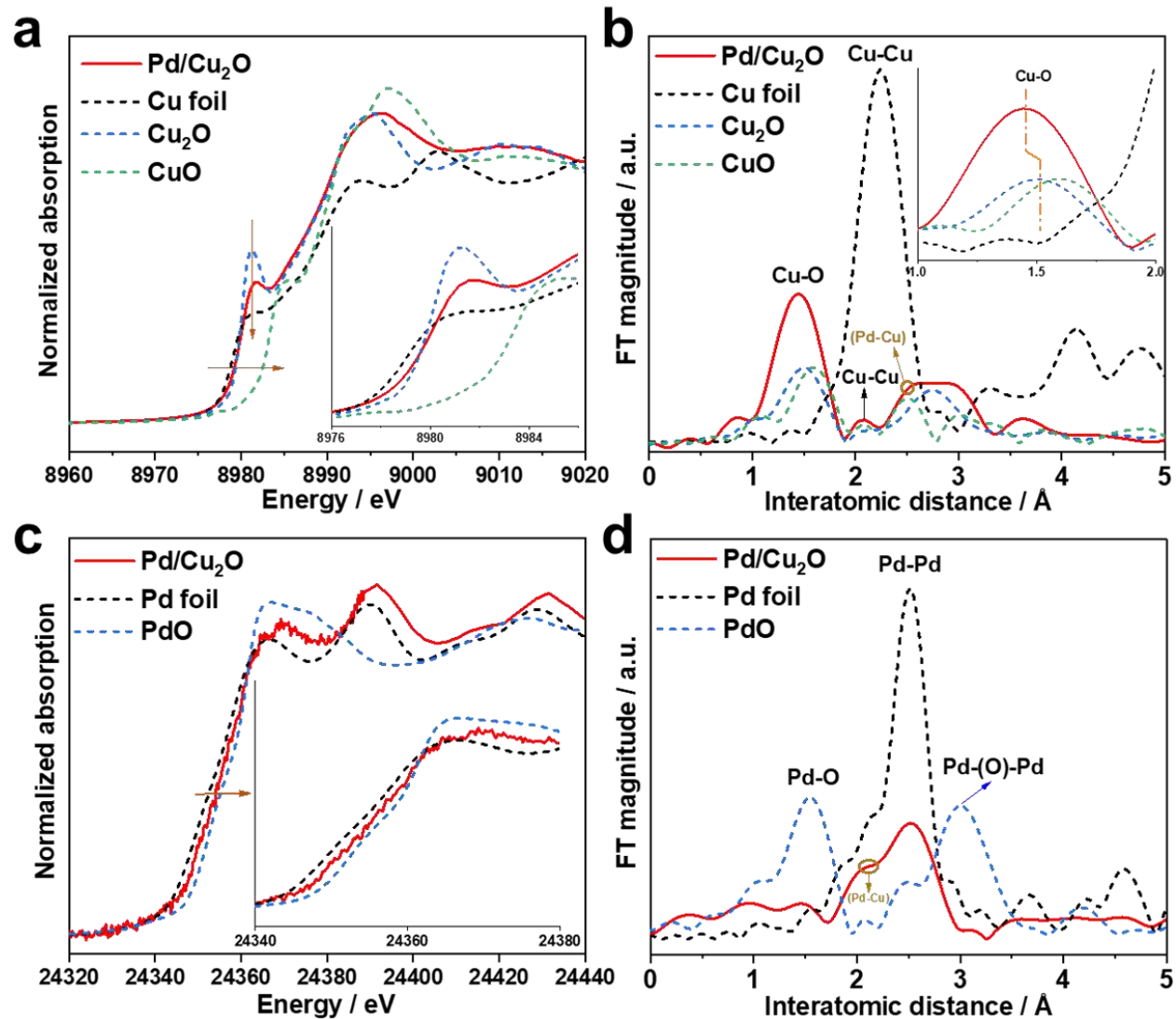
544

545



547

548 **Figure 1.** (a) Schematic illustration of the plausible formation process of mesoporous hollow
 549 sphere Pd/Cu₂O hybrids. (b) Low-magnification HAADF-STEM image, (c-d) atomic-resolution
 550 HAADF-STEM image and corresponding EDS elemental mapping images of Pd/Cu₂O hybrids.
 551 (e) TEM image and corresponding EDS elemental line scan of Cu and Pd in Pd/Cu₂O hybrids.



552
 553 **Figure 2.** (a) Cu *K*-edge XANES and (b) FT-EXAFS spectra for the Pd/Cu₂O hybrids and reference
 554 materials (Cu foil, Cu₂O, and CuO). (c) Pd *K*-edge XANES and (d) FT-EXAFS spectra for the
 555 Pd/Cu₂O hybrids and reference materials (Pd foil and PdO).

556
 557
 558
 559
 560

561 **Table 1.** EXAFS fitting parameters at the Cu *K*-edge and Pd *K*-edge for Pd/Cu₂O hybrids and
 562 references ($S_0^2 = 0.80$).

	Pd foil	Cu foil	Pd/Cu ₂ O
ΔE_0 (eV), Pd <i>K</i> -edge	1.9±0.4		0.9±2.0
ΔE_0 (eV), Pd <i>K</i> -edge		4.4±0.5	7.1±1.1
$N_{\text{Pd-Pd}}$	12		3.0±0.6
$N_{\text{Pd-Cu}}$			1.7±0.5
$N_{\text{Cu-Cu}}$		12	2.3±0.6
$N_{\text{Cu-O}}$			1.9±0.1
$\langle R \rangle_{\text{Pd-Pd}}$ (Å)	2.64±0.01		2.63±0.02
$\langle R \rangle_{\text{Pd-Cu}}$ (Å)			2.44±0.04
$\langle R \rangle_{\text{Cu-Cu}}$ (Å)		2.24±0.01	2.10±0.02
$\langle R \rangle_{\text{Cu-O}}$ (Å)			1.50±0.01
$\sigma^2_{\text{Pd-Pd}}$ (Å)	0.0057		0.0089
$\sigma^2_{\text{Pd-Cu}}$ (Å)			0.0082
$\sigma^2_{\text{Cu-Cu}}$ (Å)		0.0088	0.0082
$\sigma^2_{\text{Cu-O}}$ (Å)			0.0046

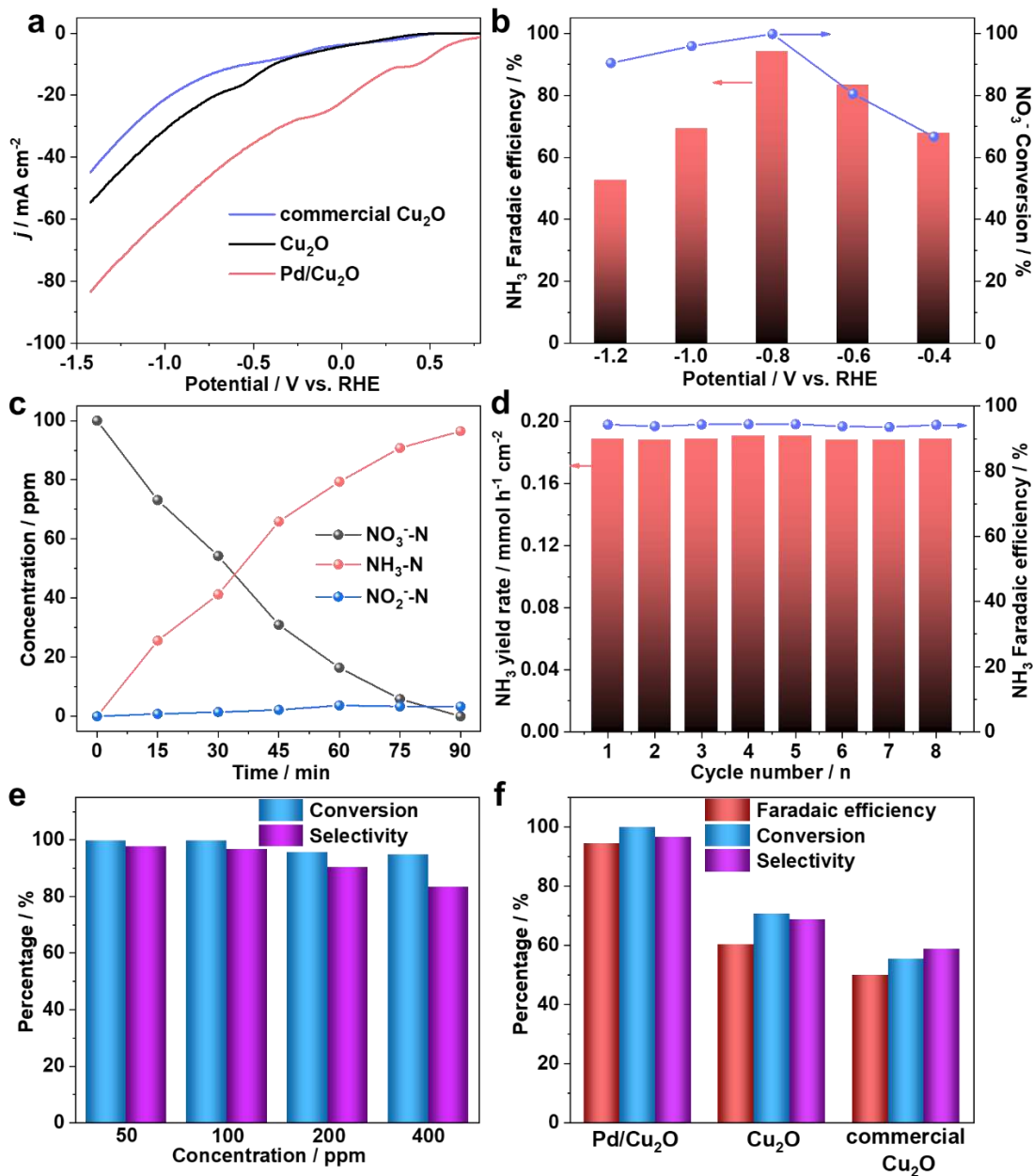
563

564

565

566

567



568

569 **Figure 3.** NO₃⁻-to-NH₃ electroreduction performances. (a) LSV curves of Pd/Cu₂O hybrids, Cu₂O,

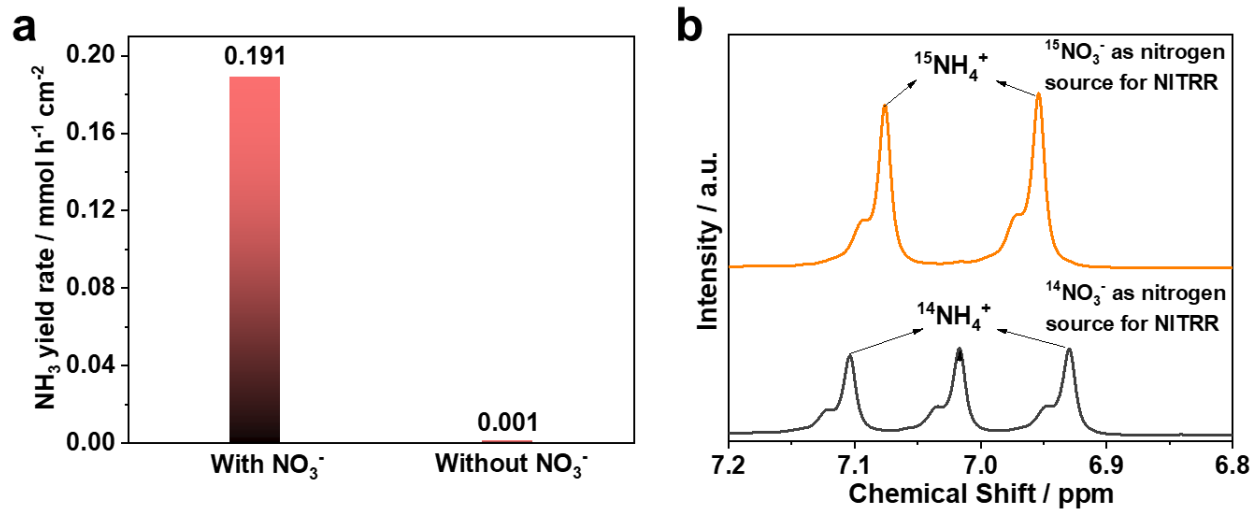
570 and commercial Cu₂O in 0.5 M Na₂SO₄ electrolyte, respectively. (b) Potential-dependent FEs of

571 NH₃ and conversion rate of NO₃⁻ over Pd/Cu₂O hybrids. (c) Time-dependent concentration change

572 of NO₃⁻, NO₂⁻, and NH₃ over Pd/Cu₂O hybrids at -0.80 V. (d) The consecutive recycling test at -

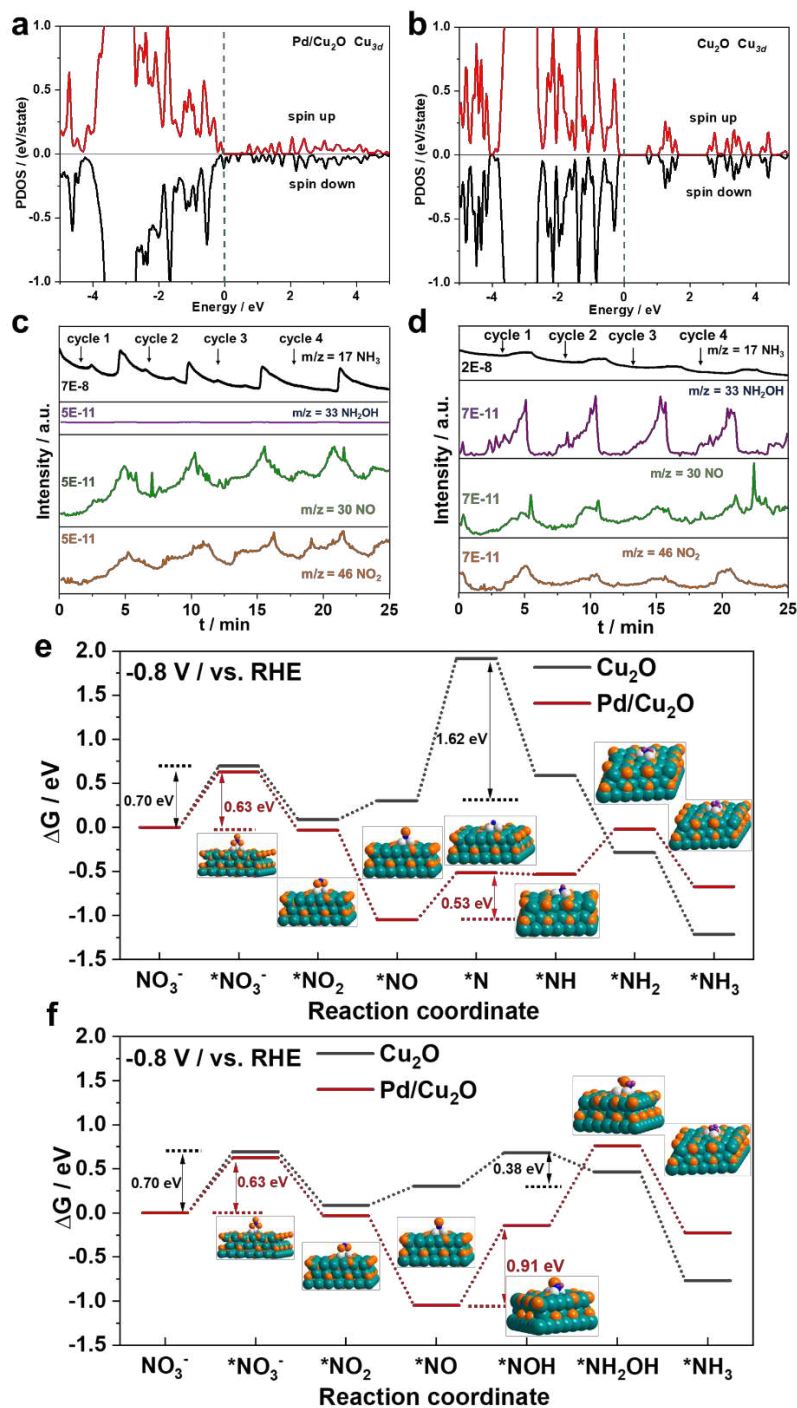
573 0.80 V over a Pd/Cu₂O cathode. (e) Conversion of NO₃⁻ and selectivity of NH₃ with different NO₃⁻

574 -N concentration. (f) FEs and selectivity of NH₃ and conversion rate of NO₃⁻ over different samples.



575
 576 **Figure 4.** (a) The NH_3 yield over Pd/ Cu_2O hybrids in 0.5 M Na_2SO_4 electrolyte with and without
 577 NO_3^- . (b) ^1H NMR spectra of the electrolyte after electrocatalytic NITRR reaction using $^{15}\text{NO}_3^-$
 578 and $^{14}\text{NO}_3^-$ as the nitrogen source.

579
 580
 581
 582
 583
 584
 585
 586
 587
 588
 589
 590
 591



592
 593 **Figure 5.** PDOS plot of Cu_{3d} orbitals in (a) Pd/Cu₂O hybrids and (b) Cu₂O. DEMS measurements
 594 of NITRR over (c) Pd/Cu₂O hybrids and (d) Cu₂O, respectively. Reaction free energies for
 595 different intermediates (e) and (f) on Pd/Cu₂O hybrids and Cu₂O, respectively. Green, orange, gray,
 596 blue, and purple represent copper, oxygen, palladium, nitrogen, and hydrogen atoms, respectively.

597 **Acknowledgements**

598 This work was financially supported by the Natural Science Foundation of China (22022605 and
599 21936005), and the China Postdoctoral Science Foundation (2020TQ0166).

600

601 **Author information**

602 **Affiliations**

603 These authors contributed equally: Haibo Yin, Yue Peng

604

605 State Key Joint Laboratory of Environment Simulation and Pollution Control, School of
606 Environment, Tsinghua University, Beijing, 100084, China

607 Haibo Yin, Yue Peng, Shangchao Xiong, Jianjun Chen, Chizhong Wang, Rong Wang, Zhen Chen,
608 Junhua Li

609

610 Division of Materials and Manufacturing Science, Graduate School of Engineering, Osaka
611 University, Osaka, 565-0871, Japan.

612 Yasutaka Kuwahara, Hiromi Yamashita

613

614 Institute of Photoelectronic Thin Film Devices and Technology, Solar Energy Research Center,
615 Key Laboratory of Photoelectronic Thin Film Devices and Technology of Tianjin, Ministry of
616 Education Engineering Research Center of Thin Film Photoelectronic Technology, Nankai
617 University, Tianjin, 300350, PR China

618 Jingshan Luo

619

620 **Contributions**

621 Haibo Yin, Yue Peng and Shangchao Xiong proposed and designed experiments. Haibo Yin and
622 Shangchao Xiong performed the experiments and analyzed data. All authors discussed,
623 commented on and revised the manuscript.

624

625 **Competing interests**

626 The authors declare no competing interests.

627

628 **Corresponding author**

629 Correspondence to Junhua Li

630

631

632

633

634

635

636

637

638

639

640

641

642

Figures

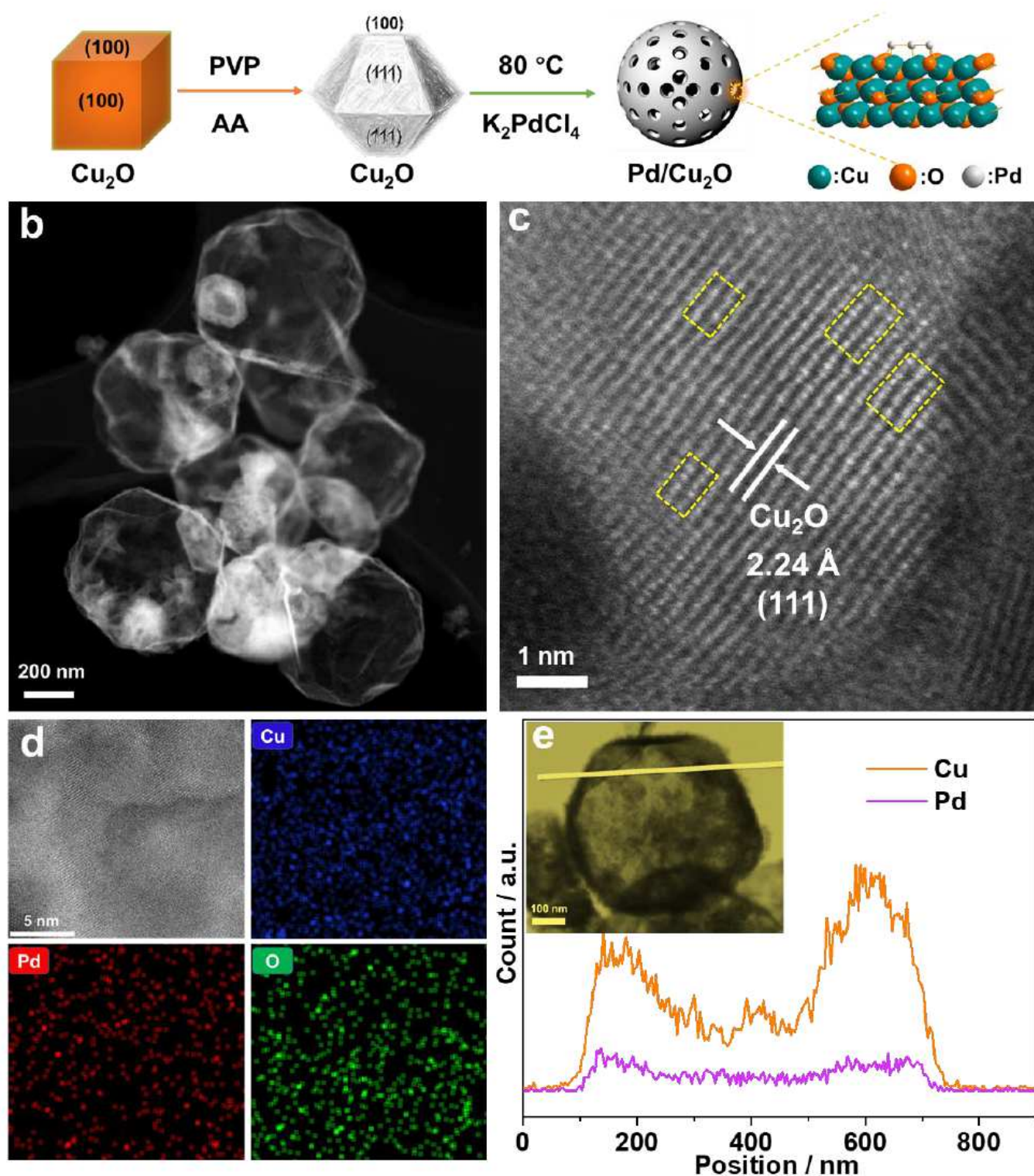


Figure 1

(a) Schematic illustration of the plausible formation process of mesoporous hollow sphere Pd/Cu₂O hybrids. (b) Low-magnification HAADF-STEM image, (c-d) atomic-resolution HAADF-STEM image and

corresponding EDS elemental mapping images of Pd/Cu₂O hybrids. (e) TEM image and corresponding EDS elemental line scan of Cu and Pd in Pd/Cu₂O hybrids.

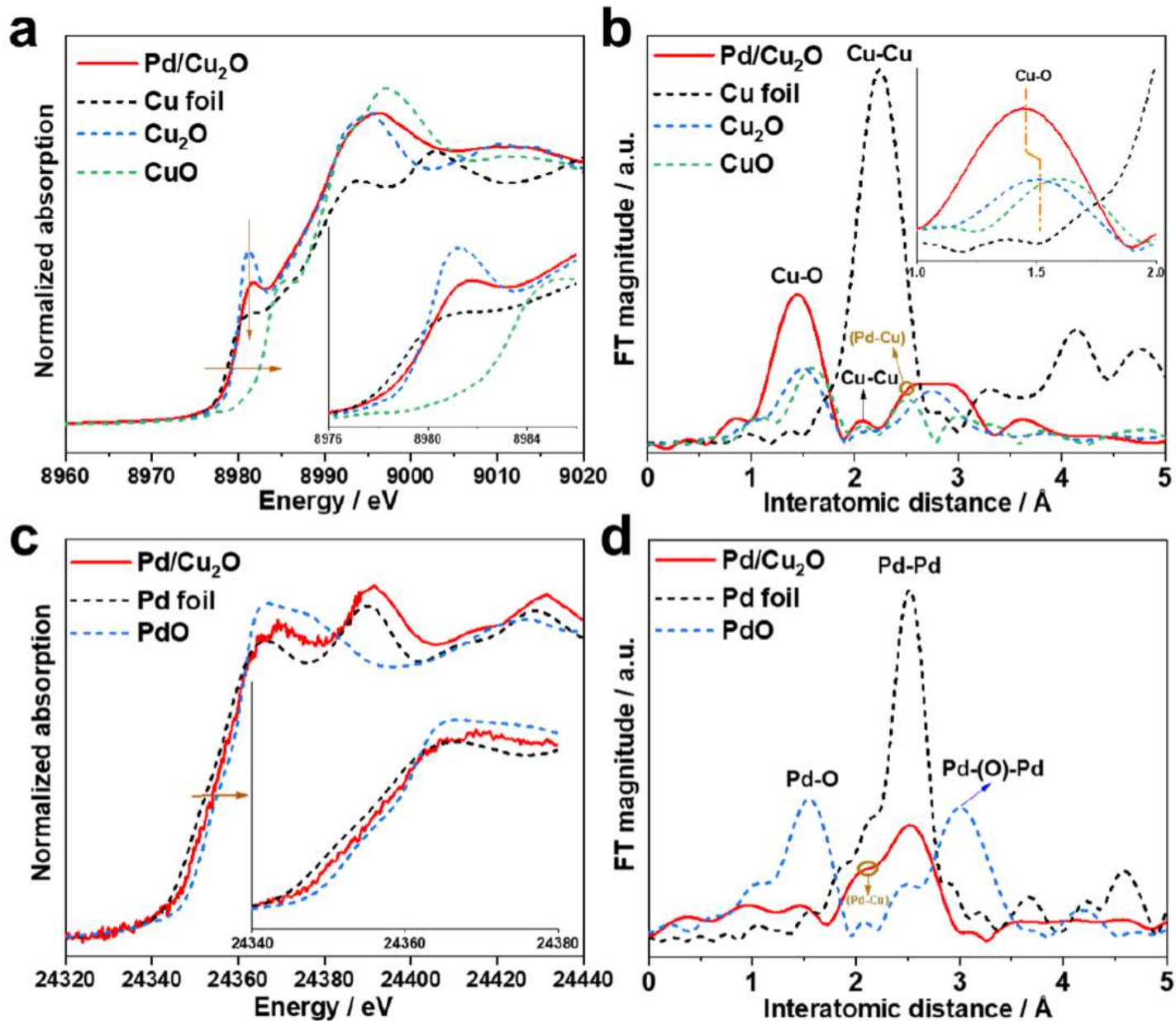


Figure 2

(a) Cu K-edge XANES and (b) FT-EXAFS spectra for the Pd/Cu₂O hybrids and reference materials (Cu foil, Cu₂O, and CuO). (c) Pd K-edge XANES and (d) FT-EXAFS spectra for the Pd/Cu₂O hybrids and reference materials (Pd foil and PdO).

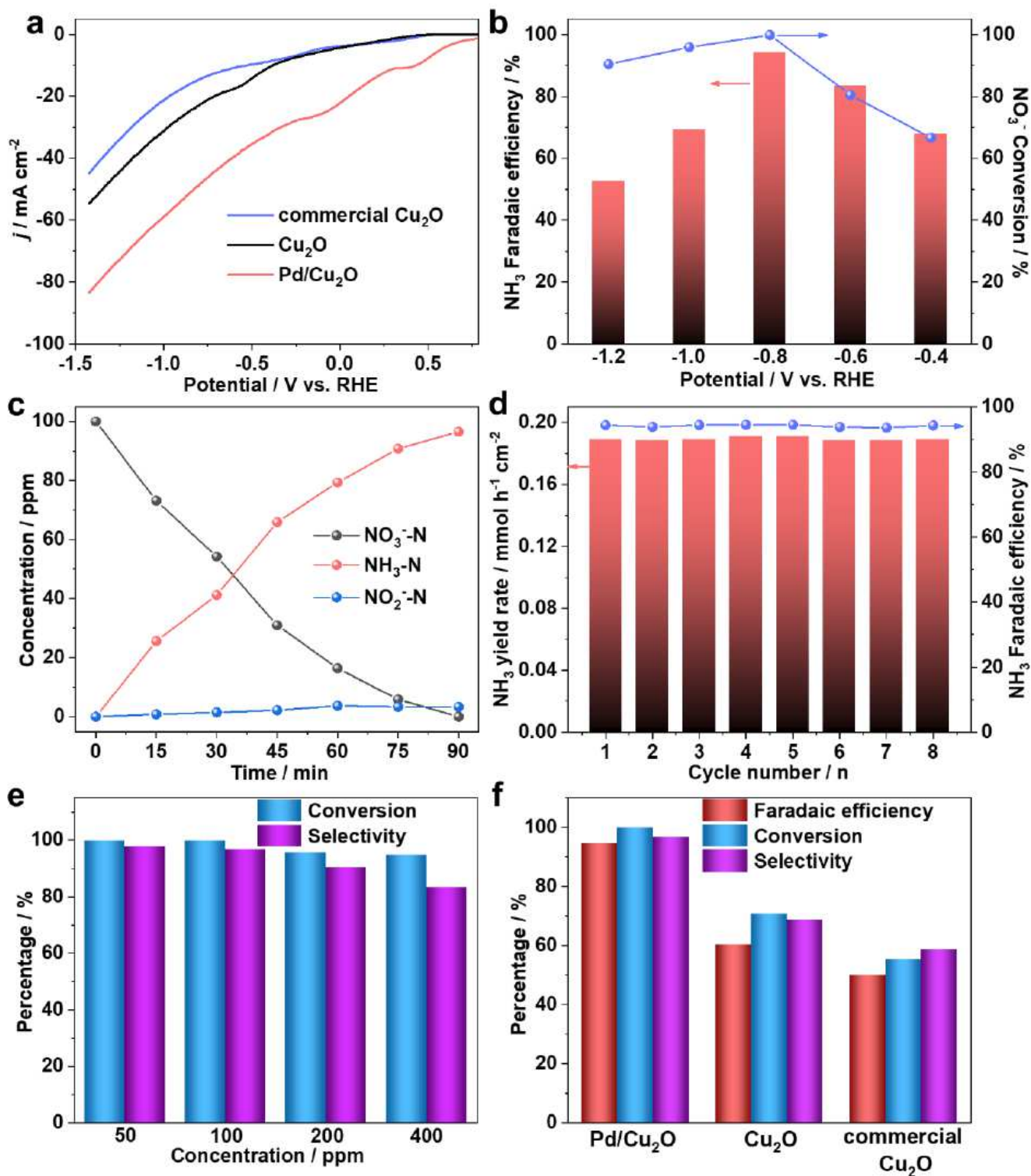


Figure 3

NO₃-to-NH₃ electroreduction performances. (a) LSV curves of Pd/Cu₂O hybrids, Cu₂O, and commercial Cu₂O in 0.5 M Na₂SO₄ electrolyte, respectively. (b) Potential-dependent FEs of NH₃ and conversion rate of NO₃⁻ over Pd/Cu₂O hybrids. (c) Time-dependent concentration change of NO₃⁻, NO₂⁻, and NH₃ over Pd/Cu₂O hybrids at -0.80 V. (d) The consecutive recycling test at -0.80 V over a Pd/Cu₂O cathode. (e)

Conversion of NO_3^- and selectivity of NH_3 with different NO_3^- -N concentration. (f) FEs and selectivity of NH_3 and conversion rate of NO_3^- over different samples.

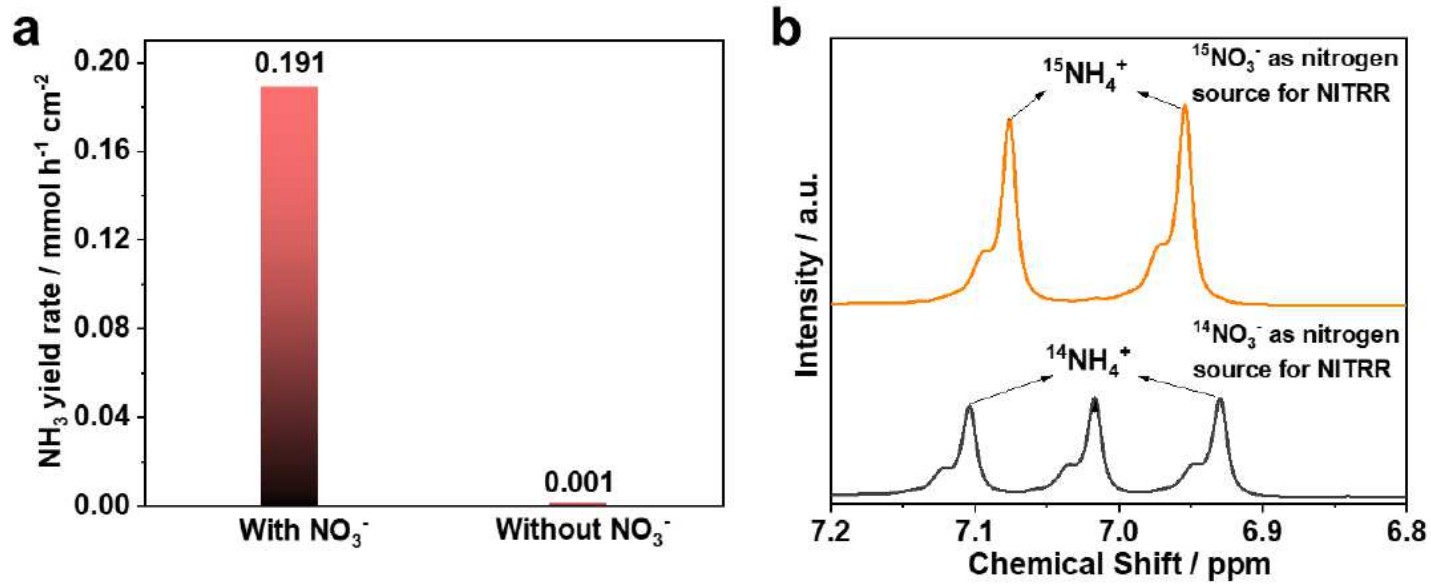


Figure 4

(a) The NH_3 yield over Pd/Cu₂O hybrids in 0.5 M Na₂SO₄ electrolyte with and without NO_3^- . (b) ^1H NMR spectra of the electrolyte after electrocatalytic NITRR reaction using $^{15}\text{NO}_3^-$ and $^{14}\text{NO}_3^-$ as the nitrogen source.

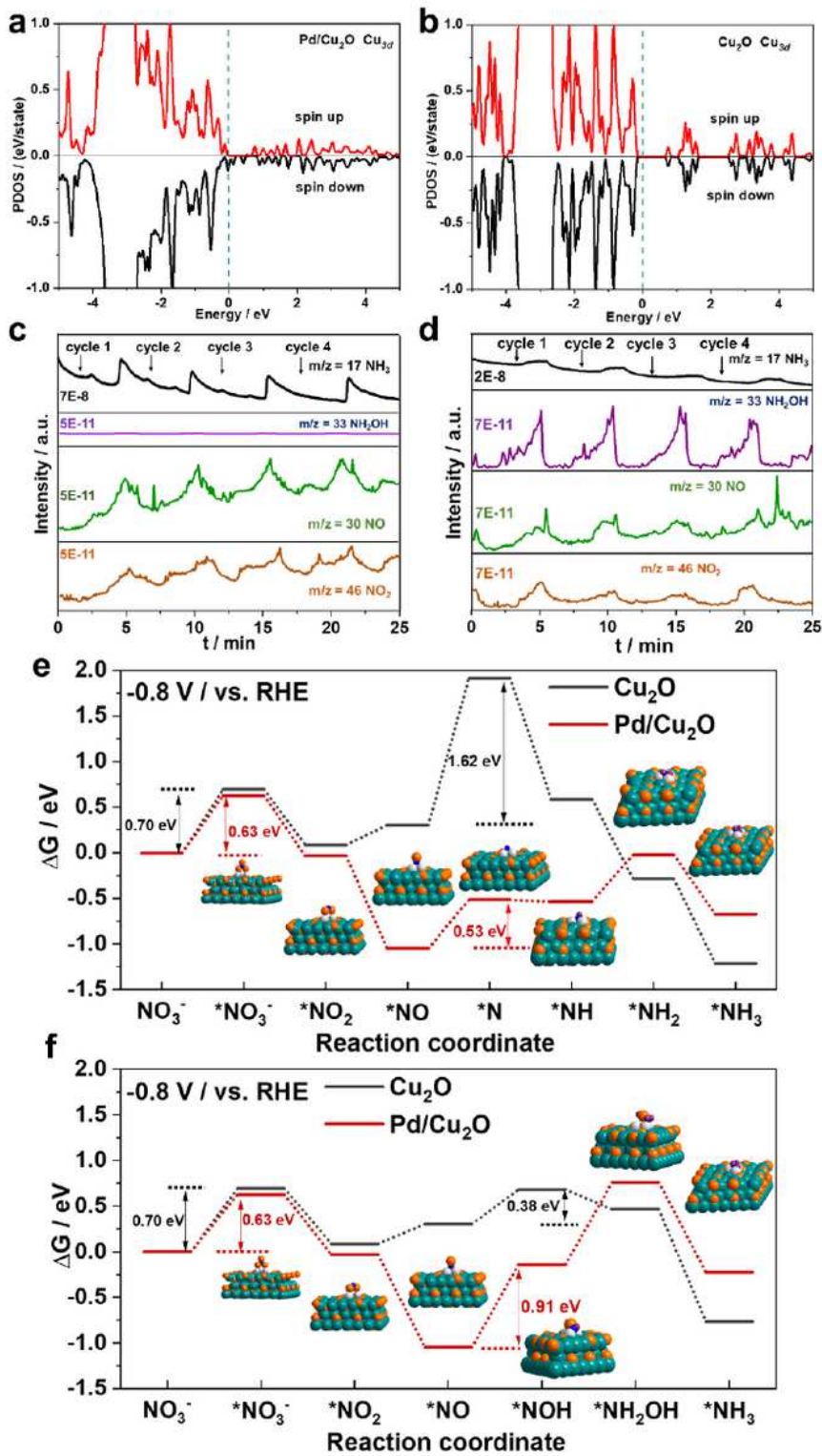


Figure 5

PDOS plot of Cu3d orbitals in (a) Pd/Cu₂O hybrids and (b) Cu₂O. DEMS measurements of NITRR over (c) Pd/Cu₂O hybrids and (d) Cu₂O, respectively. Reaction free energies for different intermediates (e) and (f) on Pd/Cu₂O hybrids and Cu₂O, respectively. Green, orange, gray, blue, and purple represent copper, oxygen, palladium, nitrogen, and hydrogen atoms, respectively.

Supplementary Files

This is a list of supplementary files associated with this preprint. Click to download.

- [Manuscriptsf.pdf](#)